Journal

J. Am. Ceram. Soc., **99** [7] 2428–2435 (2016)
DOI: 10.1111/jace.14201

The Orientation Dependence of the Photochemical Activity of α-Fe_2O_3

Yisi Zhu, Andrew M. Schultz, Gregory S. Rohrer, and Paul A. Salvador[†]

Department of Materials Science and Engineering, Carnegie Mellon University, Pittsburgh, Pennsylvania 15213

The orientation dependence of the visible-light stimulated photochemical reduction of aqueous Ag^+ on polycrystalline hematite Fe_2O_3 was determined by observing the relative amount of reduced Ag^0 on crystals of known surface orientation over all possible orientations. The results show that surfaces oriented within 20° of the $(1\bar{1}02)$ plane are the most active and surfaces close to the (0001) plane are the least active. A strong correlation is observed between the orientation-dependent activity and the orientation-dependent surface potential measured by scanning Kelvin probe force microscopy. Surfaces near the most active $(1\bar{1}02)$ plane and the least active (0001) plane are, respectively, at the most positive and the least positive ends of the potential range among all grains. The trends in activity are concluded to arise from a combination of internal fields associated with surface charges and bulk transport effects.

I. Introduction

Hematite (α-Fe_2O_3) is a promising photocatalyst because it absorbs visible light, it is inexpensive, readily available, stable in aqueous environments, and it does not contain environmentally hazardous elements. The band gap energy of 2.2 eV[1] is near the intensity maximum of the solar spectrum. While hematite can readily photo-oxidize water to generate oxygen, it cannot photoreduce water to produce hydrogen because the conduction band lies 0.21 eV below the reduction level of hydrogen. Nevertheless, hematite been widely studied as a heterogeneous photocatalyst.[2–8] Despite its promise, the photocatalytic efficiency of hematite is limited by low carrier mobilities and short carrier lifetimes.[2] Because these carrier mobilities are a function of orientation, one expects the photochemical activity of hematite to be anisotropic. Anisotropic activity can also arise from orientation-dependent surface features, including chemical terminations, reconstructions, and adsorbates, because these affect the net surface charge and the near surface space charge region. In this paper, we explore the anisotropic photochemical reduction of aqueous Ag^+ to solid Ag^0 on hematite surfaces of all orientations under visible light illumination, and demonstrate a strong correlation between the local activity to the local surface potential.

α-Fe_2O_3 adopts the hexagonal corundum crystal structure (see §1 of the supplemental material) that consists of layers of close-packed oxygen anions (O^{2-}) stacked along the *c*-axis, with iron cations (Fe^{3+}) filling two-thirds of the octahedral interstitial sites.[2] This layered structure is apparent in Fig. S1 (a). The anisotropic bonding in the hexagonal structure is reflected in the electronic properties: the measured (*n*-type) electronic conductivity along the *c*-axis is four orders of magnitude lower than along directions perpendicular to it.[9,10] As a result, the photocurrent density on orientations perpendicular to the *c*-axis is 5–10 times higher than on the basal faces.[11]

Surface properties are also expected to be strongly anisotropic. Schematic examples of ideal bulk-truncated (0001) and $(1\bar{1}02)$ surfaces are given in Fig. S1, which highlight the possibility of surfaces having different terminations and charges. While the real surfaces of hematite differ considerably from these ideal versions, their terminations still vary with orientation and they can be charged. Chemisorption of O_2 occurs in one second when the pressure is higher than 10^{-2} Torr,[12] which implies oxygen termination is likely in dry air. H_2O chemisorption occurs above 10^{-4} Torr,[13] and the partial pressure of H_2O in air varies from 0.1 to 33 Torr. Generally, there are three types of adsorbed hydroxyls: single-, double-, and triple-coordinated hydroxyls, having charge states of $-\frac{1}{2}$, 0, $+\frac{1}{2}$, respectively.[14–17] The amount and type of these hydroxyls vary with the surface orientation and preparation methods,[14–17] and further affect the local surface charge density and activity.[18]

Whatever the origin of this surface charge, it causes the near surface bands to bend in a semiconductor and generates an internal electric field that affects the driving force for photogenerated carriers to move to the surface. Examples of this band bending are shown in Figs. 1(a)–(c) for a neutral, positive, and negative surface, respectively. Each of these images are schematics of the relevant electronic energies (see caption for definitions) associated with both a sample (left side) and a nearby metallic tip (right side) to which the sample is grounded. As a result of the band bending in (b) and (c), two things occur for the positively (negatively) charged surface that favor reduction (oxidation) reactions: the population of electrons at the surface of the n-type semiconductor increases (decreases), as does the driving force for the photogenerated electrons (holes) to drift to the surface. Another consequence of band bending is that the contact potential difference between the tip and sample varies with the local surface charge, shown as E_{CPD} in Fig. 1. Smaller work function materials and more positively charged surfaces will result in a less positive (more negative) values of E_{CPD}. Kelvin probe force microscopy (KFM) is a scanning probe analytical method that yields a measure of this contact potential difference; such measurements should therefore allow correlations to be made between the local surface potential and reactivity.

The purpose of this paper is to describe the relative photochemical activity of all possible orientations of α-Fe_2O_3 and to correlate this with local surface charge. For the activity, we employ a method used earlier to study the photochemical anisotropy of $BiVO_4$[19] and TiO_2.[20] The orientations of many crystals at the surface of an α-Fe_2O_3 polycrystal were determined by electron backscatter diffraction (EBSD). Aqueous Ag^+ was then photochemically reduced to insoluble Ag^0 on the surface and the locations of reduction were correlated with the crystal orientation. The most active orientations are found to be near the $(1\bar{1}02)$ orientation, while the most inactive orientations are found close to the basal plane (0001). We then measured the relative surface potential of each plane using KFM. We find that the surface potential is strongly

---

A. Setlur—contributing editor

Manuscript No. 37285. Received July 31, 2015; revised December 9, 2015; approved February 3, 2016.

[†] Author to whom correspondence should be addressed. e-mail: paul7@andrew.cmu.edu

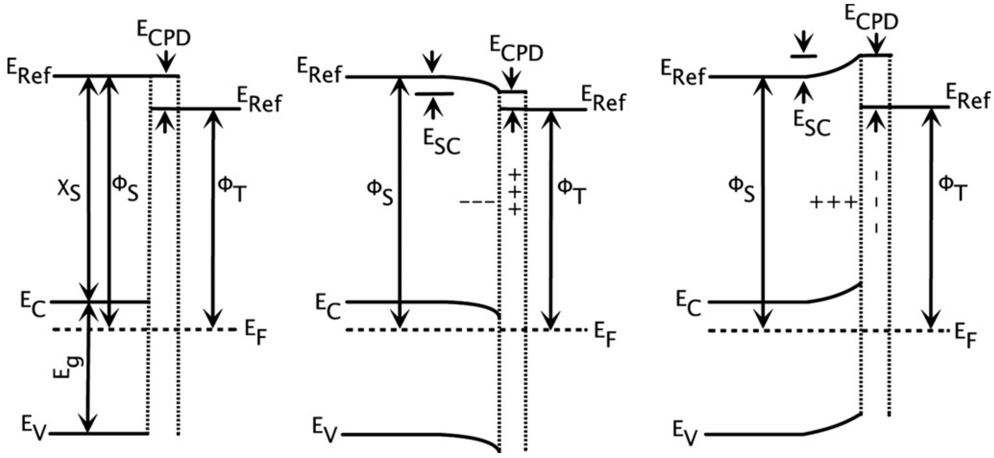

Fig. 1. Schematic electronic energy level diagrams of a sample (left side) and a conductive AFM tip (right side). The Fermi levels (E_F) are aligned and the reference level (E_{Ref}) discontinuities represent the contact potential difference (E_{CPD}). E_c, E_v, E_g, χ_S, Φ_S, and Φ_T, represent, respectively, the energies of the conduction band edge, the valence band edge, the band gap, the sample electron affinity, the sample work function, and the tip work function. The surface is (left) neutral, (center) positive, and (right) negative, with a near surface space charge region (E_{SC}) in center and right.

correlated to activity, with $(1\bar{1}02)$ having the most positive surface potential and (0001) having the least positive surface potential.

II. Experimental Procedure

Polycrystalline Fe_2O_3 was produced by conventional powder processing. Fe_2O_3 powder (99.975%, Alfa Aesar, Ward Hill, MA) was ball-milled in ethanol using yttria-stabilized zirconia grinding media (Inframet Advanced Materials, Manchester, CT). After ball-milling, a small amount (typically 1–2 wt%) of polyethylene glycol (PEG, ~8000 g/mol, Alfa Aesar) was added as a binder, and mixed thoroughly. Pellets of the dried powder were formed under uniaxial loads in a 1-cm diameter stainless steel die. After pressing, the pellets were loaded into an alumina crucible, heated in air to 600°C at 10°C/min, and held at 600°C for 12 h to burn off the binder. They were then heated to 1200°C at 5°C/min, sintered for 48 h at 1200°C, and finally cooled in air at 10°C/min. The sintered samples were lapped flat using a 3 μm alumina suspension and then chemomechanically polished using a 0.03 μm alumina suspension. The polished samples were annealed at 1100°C for 6 h in air to repair polishing damage and etch the grain boundaries (heating and cooling rates were 10°C/min).

The orientations of the surface grains were determined using EBSD. EBSD patterns were acquired using a Quanta 200 SEM (FEI, Hillsboro, OR) with the sample tilted to 70° and with an accelerating voltage of 25 kV. Patterns were automatically analyzed and indexed using TSL data collection and analysis software (EDAX, Mahwah, NJ).[21,22] Several steps of data cleaning were applied. First, pixels having a low confidence index ($CI < 0.1$) were removed from the data set, typically arising from grain boundaries, surface pores, or scratches. Then, the EBSD data were cleaned using a single iteration of grain dilation, using a minimum grain size of 50 pixels and a disorientation angle threshold of 5°. Finally, each pixel of a grain was assigned the average orientation for that grain.

The photochemical reduction of aqueous Ag^+ to solid Ag^0 was carried out as described previously.[7,19,20,23,24] A Viton O-ring (diameter ~1 cm) was placed on top of a hematite pellet, 0.115 M $AgNO_3$ aqueous solution was poured into the O-ring, and a quartz slip was then placed on top, sealing the solution in the O-ring by capillarity without an air bubble. The assembly was illuminated using a commercially available blue LED operated at 750 mA ($\lambda_{peak} = 470$ nm, Philips Lumileds, San Jose, CA) for up to 20 min. After reaction, the samples were rinsed with deionized water.

The surfaces were examined before and after photochemical reaction with optical, atomic force microscopy (AFM), and KFM. Conventional AFM images were obtained using an Ntegra or Solver Next AFM (NT-MDT, Moscow, Russia). Aluminum-coated silicon tips (NSG10, NT-MDT) having a rated resonant frequency of 240 Hz were used for semicontact mode imaging. The local surface potential of active and inactive grains was measured using KFM (with the sample covered and not exposed to ambient light sources) with either NSG03 tips coated by Pt/Ir or 190E-G tips coated by Cr/Pt ($\Phi \approx 5.1$ eV). A lengthy description of the KFM measurements is given in the supplemental information (§ 2). Briefly, KFM is a two-pass semicontact mode technique. The first pass acquires the sample topography. During the second pass, the tip is maintained (using the topography information acquired during the first pass) at a user-defined distance (10 nm) above the sample surface, and a dc-bias V_{SP} is applied to offset the Coulomb force. V_{SP} is related to the contact potential difference (shown in Fig. 1): $V_{SP} = -a \times E_{CPD}/e$, where a is a constant that relates to the scan settings ($0 < a < 1$). Because V_{SP} has the opposite sign to E_{CPD}, smaller work function materials and more positively charged surfaces will result in a more positive values of V_{SP}.

Finally, we used a Au ($\phi = 5.1$ eV) – Pt ($\phi = 5.7$ eV) standard sample to calibrate the KFM for every experiment. While V_{SP} should be more positive for Au than for Pt,[25,26] most of the time (≈70%) we observed Pt to be more positive than Au. In these cases, the relative V_{SP} values for the Fe_2O_3 ($\phi \approx 5.5$–5.6 eV[11,27]) grains were inverted too. The reasons for the inversion were not resolved, but could arise from variations in the tip, machine set up, or environmental conditions.[28–31] Herein, we report only data from datasets exhibiting inverted control values because these represented the majority (70%) of experiments. The values reported herein were corrected (sign inverted) such that they agree with the expectations for the controls (presented above for E_{CPD} and V_{SP}).

III. Results

Two characteristic topographic AFM images are shown in Fig. 2, which were recorded after a 10 min photochemical reaction. Bright (dark) regions are topographically high (low). The dark interconnected lines arise from the thermally grooved grain boundaries. The relatively uniform intermediate contrast enclosed by the grain boundaries arise from the relatively smooth surfaces of individual grains. The small bright features arise from particles of photodeposited silver, which was confirmed using energy-dispersive spectroscopy in a scanning electron microscope and X-ray diffraction.

It is immediately clear that not all grains have the same relative activity for Ag$^+$ photoreduction, based simply on the relative number or total amount of bright particles on different grains. We classified the relative activity into three groups: highly (denoted with “H”), moderately (denoted with “M”), or poorly (grains unmarked in Fig. 2) active. The classification was based on the relative area of the grain surface that was covered with bright particles. H (M) grains exhibited Ag^0 particles uniformly spread across their surface covering over 10% (between 2% and 8%) of the total grain area. Poorly active grains either had no observable Ag^0 particles, or a few randomly distributed particles covering less than 1% of the grain area. We recorded 11 similar AFM images (each 30 μm × 30 μm) from different regions on the surface after silver photoreduction, and classified their grains in an identical fashion. Overall, we characterized 69 grains for activity using AFM images, with 21 (or 30%), 20 (or 29%), and 28 (or 41%) classified as highly, moderately, and poorly active, respectively.

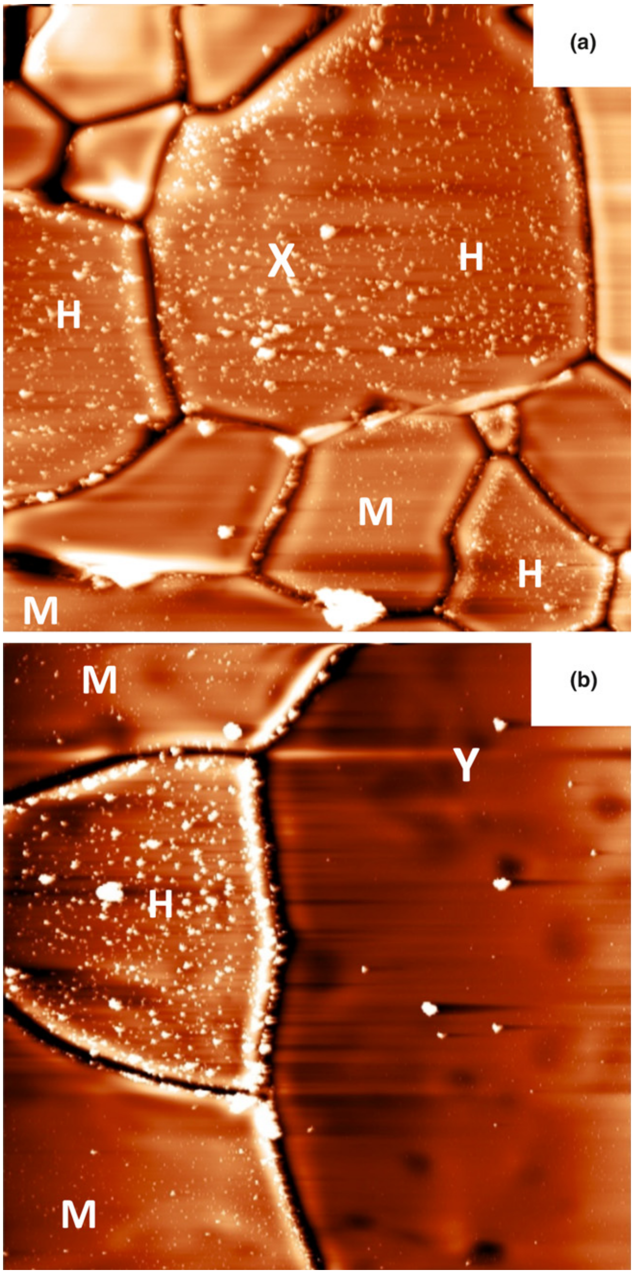

Fig. 2. (a) and (b) are both representative AFM images of α-Fe$_2$O$_3$ surfaces after silver reduction. Grains classified as highly (moderately) active are marked “H” (“M”), while inactive grains are unmarked. Grains marked with “X” and “Y” identify common grains with Fig. 3. The size of each image is 30 μm × 30 μm.

The orientations of the surface grains that were classified for their activity were then determined using EBSD. In the inverse pole figure (IPF) map given in Fig. 3, each pixel is colored according to the orientation of the local surface normal (the legend is given as an inset). Regions of constant color correspond to grains of constant average orientation. For reference, the regions shown in Fig. 2 (Fig. 5) are marked and outlined by white squares (red rectangle) in Fig. 3.

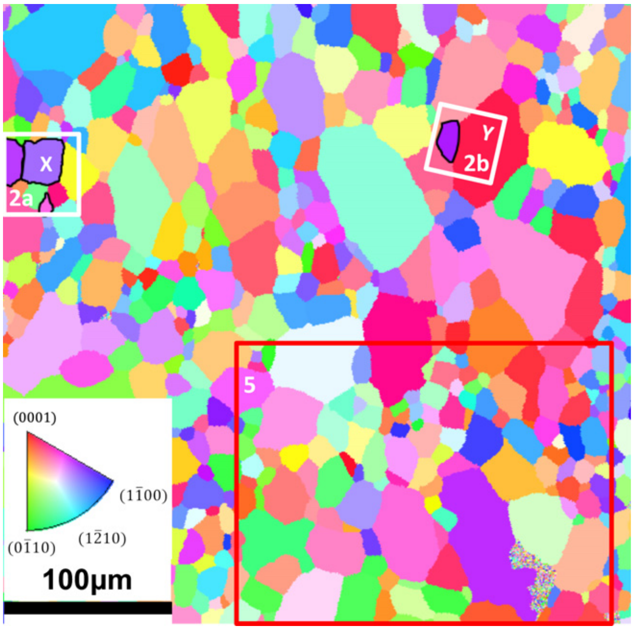

Fig. 3. Inverse pole Fig. (orientation) maps of the α-Fe$_2$O$_3$ surface. The color code is given as the standard stereographic triangle of a hexagonal crystal. Grains marked with “X” and “Y” identify common grains with Fig. 2. The white (red) boxes indicate the regions shown in Fig. 2 (Fig. 5). Highly active grains from Fig. 2 are outlined by black lines.

The activity of different grains is plotted versus their orientation on a stereographic projection in Fig. 4. The symbols correspond to the relative activity of each grain. Most of the 21 highly active grains (red solid triangles) are clustered near the $(1\bar{1}02)$ orientation. While most of the grains near $(1\bar{1}02)$ are highly active, not all are. More than half of the poorly active grains (open circles) are within 40° of the (0001) orientation: 17 of the 28 existing in the angular space of the triangle from (0001) to $(0\bar{1}14)$. Most of the poorly active grains are away from $(1\bar{1}02)$ orientation, with one outlying poorly (highly) active grain overlapping (outside) the region of orientation space in which the highly active grains mainly exist. The moderately active grains are spread in orientation space, but they mainly separate the regions of highly and poorly active grains, while having a significant overlap with these other clusters.

While AFM is a good indicator of the initial activity, owing to its high sensitivity to topographic variations, it is time-consuming to generate significantly larger data sets. As such, dark-field (DF) optical microscopy (OM) was used to quantify the relative coverage of silver particles on a much larger set of grains spread over a much larger area. Figure 5(a) is a DF-OM image of the Fe$_2$O$_3$ surface after the photochemical reduction of silver (for 20 min). In the image, the grain surfaces appear dark, while the grooves at the

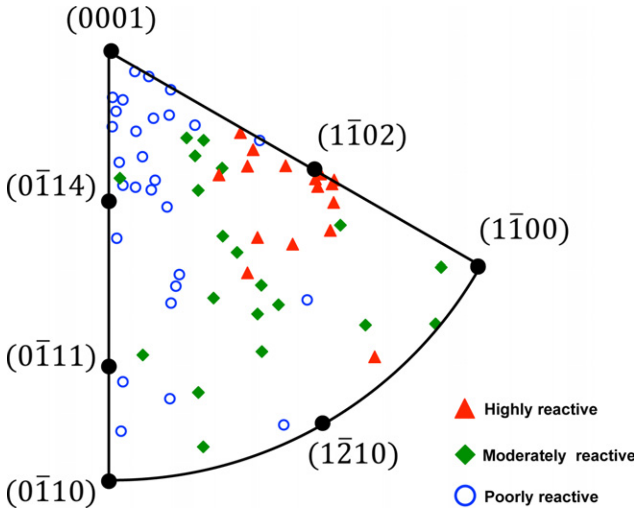

Fig. 4. Orientation-dependent activity (as determined from AFM measurements) of 89 grains plotted on the standard stereographic triangle for hexagonal crystals. Each point indicates the activity classification (see legend) and the location in the triangle represents the orientation.

boundaries and the silver nanoparticles appear bright. The corresponding area is marked by the red rectangle in Fig. 3. To improve the contrast in the image and to quantify the activity, the DF-OM images were further analyzed using Photoshop and Matlab. First, the reacted surfaces were converted to gray scale images (0–255 levels). Then, pixels with gray scale values more than 6 greater than the average of neighboring pixels, which belong to reactants or grain boundaries, were set to white (level 255). The image after this processing is shown in Fig. 5(b). An AFM topography image is shown in Fig. 5(c), which was taken from the region outlined with a red rectangle in Fig. 5(b). The processed DF-OM from this region is shown in Fig. 5(d). Comparing Figs. 5(c) and (d), there is very good correlation between the bright silver particles in AFM and the white pixels (away from the grain boundaries) in the processed DF-OM image. As such, it is reasonable to assign the white pixels in the DF-OM, away from the grain boundaries, as representing silver particles on the hematite surfaces.

We again classified the relative activity of grains by quantifying the percentage of each grain covered by Ag^0, as indicated by the percentage of white pixels on the each grain surface (away from the boundaries) in the processed DF-OM images. Four DF-OM images were used, taken from regions also characterized with EBSD; the data set contained 547 grains (compared to the 69 used in the AFM dataset). The percentage of white pixels varied from 0% to 46.5%. Finally, the activity was classified as poorly, moderately, and highly active when the silver coverage (white pixel percentage) was 0%–3%, 3%–20%, and more than 20%, respectively. This resulted in the assignment of 247 (or 45%), 234 (or 43%), and 66 (or 12%) for poorly, moderately, and highly active grains, respectively.

The relative activity of these 547 grains (based on the DF-OM analysis) is plotted versus their orientation on a stereographic projection in Fig. 6. The relative activity distribution shown in Fig. 6 is similar to the result from AFM analysis (in Fig. 4), and there is a considerable overlap between the moderately active grains and the other classifications. Still, the highly active grains are clustered around the $(1\bar{1}02)$ orientation, with a few extra outliers in this larger dataset. Also, almost every grain near the $(1\bar{1}02)$ orientation is either highly or moderately active. Grains near (0001) are almost exclusively poorly active; over 90% of the grains within 30° of the (0001) plane are poorly active (most grains within the angular space of the triangle from (0001) to $(0\bar{1}14)$ are poorly active). Grains in the region nearby the triangle edge from (0001) to $(0\bar{1}10)$ are generally inactive, with the number of moderately active grains increasing in this region on moving away from the (0001). In the remainder of the triangle, the moderately and poorly active grains are intermingled. However, the number of moderately (poorly) active grains increases (decreases) on moving from the region near $(0\bar{1}10)$ to the region near $(1\bar{1}00)$.

KFM measurements were used to quantify the surface potentials of the grains investigated with the DF-OM analysis. A representative example of these results is shown in Fig. 7. The potential and topographic images recorded from a clean surface are shown in Figs. 7(a) and (b), respectively. The processed DF-OM image from this region, after reaction, is shown in Fig. 7(c). Two active grains covered by silver, and portions of five adjacent poorly active grains are shown in the DF-OM image. The active grains have measured KFM potentials [Fig. 7(a)] that are more positive (less negative) than the poorly active ones.

There is a significant variability in the KFM measurements taken from many different images because the absolute potential value (even from a single grain) varies with the tip shape, the coating type, wear of the probe, as well as instrumental and environmental factors. To analyze the data consistently and to be able to compare different images, we used the following procedure. First, we determined the average surface potential of an image, excluding the grain boundaries [for the image in Fig. 7(a), this value is –159 mV]. Then, we determined the average surface potential of each grain in the image [for the image in Fig. 7(a), the value of the two active grains are –135 and –153 mV]. These steps were carried out using the Gwyddion software package. Finally, we determined the difference between the grain's average value and the image's average value [for the image in Fig. 7(a), the value of the two active grains are +24 and +6 mV]. Using this approach, we can compare the relative surface potential of individual grains taken from many different KFM images.

We carried out this procedure on 167 separate grains in 16 separate KFM images, where the scan areas varied from 30×30 μm^2 to 80×80 μm^2. The range in relative surface potential values for all grains was from –35 to +45 mV (all values being relative to the average potential in the image from which they were taken). The orientation dependence of the measured relative surface potential is given in Fig. 8(a). For simplicity of presentation, we segmented the stereographic projection into 39 regions, separated along a 10° grid line for the hexagonal system, and plot the number average relative potential of all grains in the region. There are an average of ≈ 4 grains per region, with the lowest having 1 and the highest having 9 grains. Orientations within 30° from the (0001) plane are at one extreme of the potential range, having the least positive relative surface potential. Orientations within 30° of the $(1\bar{1}02)$ plane are at the opposite potential extreme, having the most positive relative surface potential.

The absolute activity (not using the classification scheme of Fig. 6) of the 547 grains from the DF-OM analysis is plotted in Fig. 8(b) versus their orientation on the same stereographic projection given in Fig. 8(a). The values plotted are the number average percentage of Ag coverage (white pixels) for all grains in the region, according to the color legend in the figure. There is a very strong correlation between the relative activity (absolute coverage of Ag) and the extremes in the measured relative surface potentials: grains close to the (0001) orientation are the most inactive grains and they have the most negative surface potential values, while grains near $(1\bar{1}02)$ are the most active grains and they have most positive surface potentials. It should be pointed out that outliers were observed: not all active grains had positive surface potentials (though most did), and not all grains with large positive surface potentials were active (though most were).

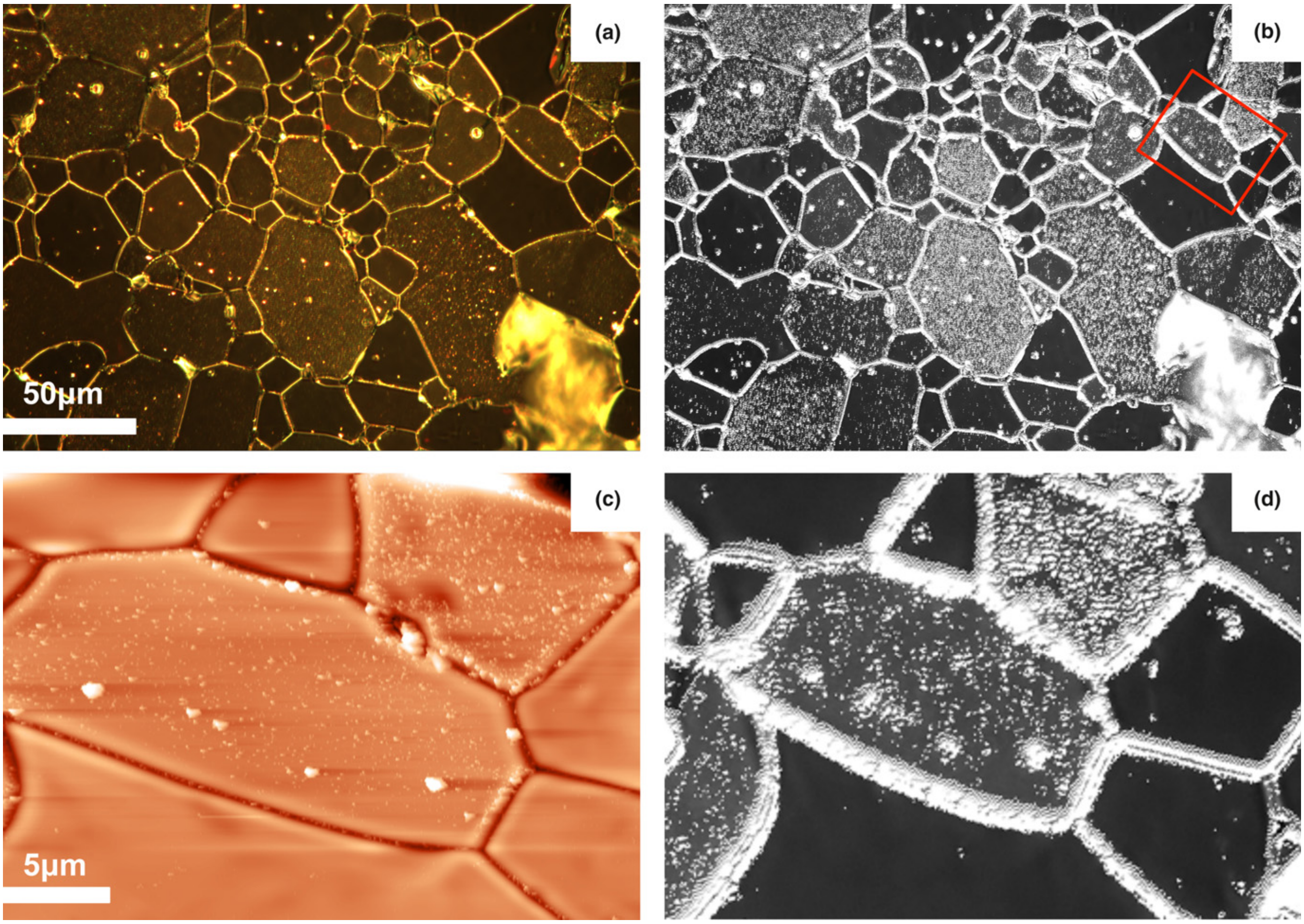

Fig. 5. Dark-field optical microscopy images of the α-Fe_2O_3 surface (corresponding to the grains in the red rectangle in Fig. 3) after the photochemical reduction of Ag. The unprocessed image is given in (a) and the processed image (see text) in (b). The red box in (b) outlines the region from which the AFM topographic image, given in (c), and the magnified processed DF-OM image, given in (d), are taken.

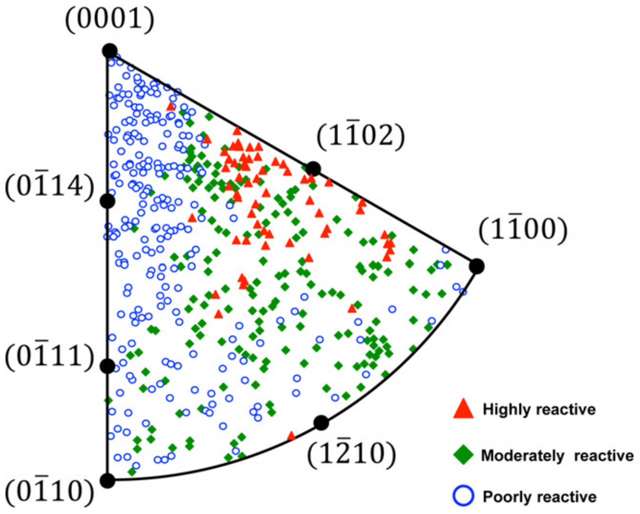

Fig. 6. Orientation-dependent activity (as determined from optical microscopy measurements) of 547 grains plotted on the standard stereographic triangle for a hexagonal crystal. Each point indicates the activity classification (see legend) and the location in the triangle represents the orientation.

A number of experiments were conducted to test the reproducibility of the observations and the sensitivity to the experimental conditions. First, a surface layer thinner than the average grain size was removed by polishing, and the high-temperature thermal etching treatment was repeated. When the reduction reaction was also repeated, the same grains were active. Second, KFM images recorded after an extended immersion in water and KFM images recorded after drying at 120°C were compared: there were no significant differences in the measured relative surface potentials between these experiments. Third, when the silver was removed from the surface after the reaction, the measured relative surface potential was the same as that measured before the reaction. Finally, samples were annealed under different temperatures and using different times. Most often we found the results described above, and we always found a correlation between activity and surface potentials, the primary observation of this work. Also, the (0001) was always the least active orientation and had the least positive surface potential. However, we did observe that the orientation of the highly active grains with the most positive surface potentials was sometimes found to be within 15° of the $(1\bar{2}10)$ prismatic plane, for a small number of samples. This phenomenon is possibly due to a different surface reconstruction and surface absorption layer for samples processed in different conditions.

IV. Discussion

The results show that the photochemical activity of α-Fe_2O_3 for the reduction of aqueous Ag^+ to solid Ag^0 is strongly anisotropic, as are the measured KFM surface potentials. Surfaces oriented near (0001) are significantly less active than other orientations, while surfaces oriented near $(1\bar{1}02)$ are significantly more active than others (for samples annealed at 1100°C). The measured KFM surface potentials are strongly

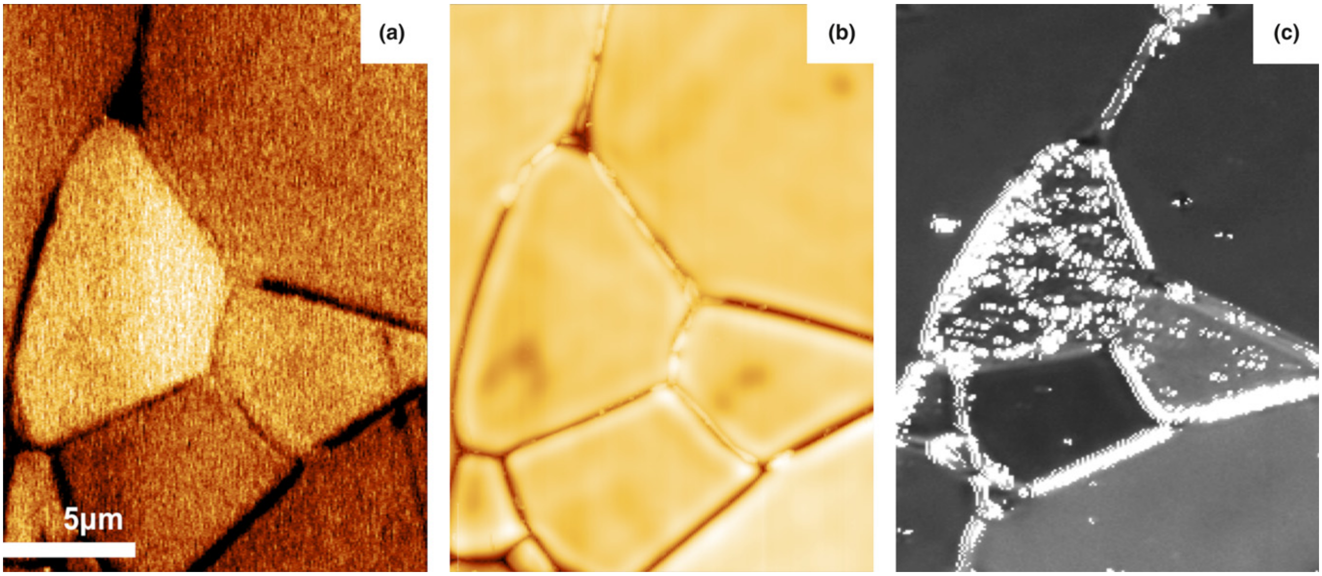

Fig. 7. A representative KFM image (a) and the associated AFM topography image (b), as well as the DF-OM image after reaction (c). The horizontal scale is the same in all images, given in (a). The color range in the KFM image runs from –220 mV (dark) to –100 mV (light), and in the AFM image from 0 nm (dark) to 200 nm (light).

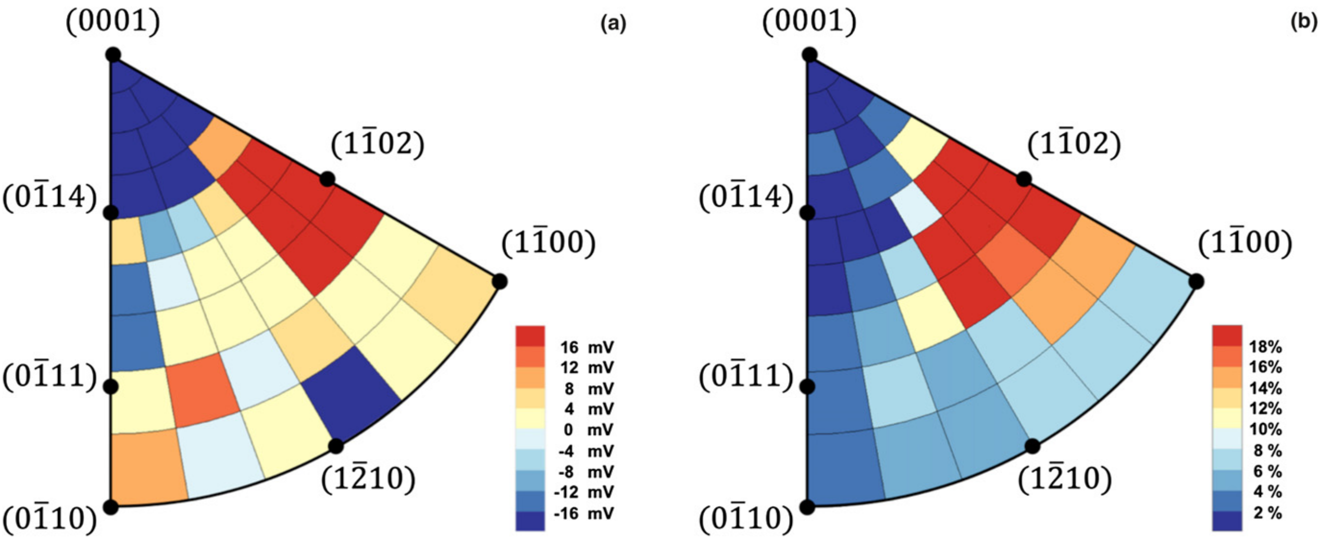

Fig. 8. (a) The average relative potential value (see text) measured by KFM (for 167 grains from 16 different images) plotted versus orientation on a stereographic projection broken into 39 regions. (b) A similar plot of the average activity (see text) measured from DF-OM images (for 547 total grains).

correlated with the activity: surfaces oriented near (0001) have less positive surface potentials than other orientations, while surfaces oriented near $(1\bar{1}02)$ have more positive surface potentials than others.

The idealized bulk-truncated surfaces of the $(1\bar{1}02)$ plane were depicted in Fig. S1(b). The oxygen terminated surfaces depicted in Fig. S1(b) would be neutral or negatively charged, in contrast to the observations. The $(1\bar{1}02)$ plane is reported to be hydrated and $\approx$ 75% of the absorbed water molecules are dissociated at surface.[32,33] The hydrated surfaces are also reported to be positively charged in a $pH < 8.5$ environment,[32,34] which is in accordance with the KFM measurements that indicate the surface is positively charged. The hydrated (0001) plane is predominantly terminated by doubly coordinated hydroxyls,[35] which are relatively inert to the protonation–deprotonation reactions, and is reported to be more negatively charged compared to all other prismatic and rhombohedral planes under acidic to neutral conditions.[11,35,36] Our KFM observations are generally consistent with these earlier reports, and the reactivity is well correlated with the measured surface charge.

The anisotropic photochemical properties of oxides can arise from both bulk and surface properties. Past studies focusing on the anisotropic properties of hematite α-Fe_2O_3 have focused on bulk property differences between basal (perpendicular to the *c*-axis) and prismatic planes (parallel to the *c*-axis). As noted earlier, photocurrent densities measured for prismatic surfaces are larger than basal surfaces.[11] This was attributed to the greater electronic conductivity parallel to the basal plane, which improved the electron-hole separation and therefore decreases recombination. While the low conductivity (and associated low mobility of carriers) along the [0001] direction of hematite is consistent with the poor activity of its basal plane, these bulk properties alone cannot explain why the $(1\bar{1}02)$ has the highest activity. The bulk conductivity favors activity on the prismatic faces, which have normal in directions of highest conductivity,[37] not on the $(1\bar{1}02)$ face.

It is possible that anisotropic light absorption, relative to the momentum of the photogenerated carriers, affects the overall activity, as proposed for $SrTiO_3$.[38] A calculated band dispersion diagram for hematite Fe_2O_3 is shown in Fig. S2.[39] This anisotropic absorption (see § 3 of supplemental) behavior further reinforces an expected low activity of (0001) because the direct band gap for electrons traveling perpendicular to this face is 0.3–0.5 eV larger than for electrons traveling toward the prismatic and rhombohedral faces. This would result in fewer photogenerated carriers traveling in these directions, and a resultant lower activity. However, one expects no significant difference in electron populations (based on band gap absorption) for directions normal to $(1\bar{2}10)$, $(1\bar{1}00)$, and $(1\bar{1}02)$. Again, while the anisotropy of this bulk property supports the poorly active nature of the (0001) basal plane, it cannot explain the higher activity of the $(1\bar{2}10)$ plane compared to the prismatic planes.

Reports[40–43] suggest that the increased activity of certain orientations of TiO_2 results from the presence of certain highly active surface planes. The anisotropic activity of $SrTiO_3$ has been attributed both to the differences in the energies needed to create electron–hole pairs with momentum along different crystallographic directions[38] and to differences in surface polarity.[23] Surface polarity from internal polarization in ferroelectrics has also been shown to be an important factor in local activity.[24,44–46] More recently, it was shown that centrosymmetric ferroelastics can exhibit surface polarizations that directly affect surface photochemical reactions.[47] The correlation observed here for Fe_2O_3 between the anisotropic surface potential measured with KFM and the anisotropic activity indicate that surface charges play a significant role in determining the local photochemical activity. A similar effect was reported for ZnO, for which the high photochemical activity of the (110) plane was ascribed to greater upward band bending and higher surface conductance.[48]

Fig. 1 depicts the energy band diagram of hematite surfaces with different surface charges, in the dark. Assuming the illumination is low enough such that the photogenerated carrier populations are much lower than the background, these diagrams will be appropriate to describe reaction conditions. Because the conduction band of hematite is 0.21 V vs. NHE,[39] it lies 0.59 eV above the reduction level of silver (0.8 V, not shown in diagram). Therefore, band edge electrons at the surface have significant excess energy towards the silver reduction reaction, regardless of that surface charge (or type of band bending). Therefore, the population of photoelectrons at the surface controls the silver reduction activity.

A positively (negatively) charged surface is expected to increase the downward (upward) surface band bending, leading to an increase (decrease) in the electron population in the near surface space-charge region and to an internal electric field that helps photogenerated electrons (holes) drift to the surface. Therefore, a positively charged surface is expected to be more reactive for photoreduction as the population of electrons (native and photogenerated) is larger. The highly active $(1\bar{1}02)$ surfaces have the most positive surface charges, while the poorly active (0001) surfaces have the most negative surface charges. The idea that the active grains have a more positive surface potential is supported by the KFM measurements: highly active grains were on average 60 mV more positive than poorly active grains. While the magnitude of this difference is affected by a variety of screening phenomena, and the value should not be interpreted as an absolute difference in surface potential, it can be interpreted as a relative difference in surface charge. Such modifications of activity based on the surface band bending are analogous to the photochemical reaction on ferroelectrics, where positive domains reduce solution species and negative domains oxidize them. In contrast to the bulk properties that explain poor activity of the basal plane, the surface charge correlates strongly with the activity across all of orientation space, indicating that it contributes strongly to the relative activity of all surfaces of hematite. This indicates that control of surface charges is an attractive approach to optimizing the activity of photocatalysts.

V. Conclusions

Experimental observations indicate that surfaces of α-Fe_2O_3 (annealed at 1100°C) oriented within 30° of the $(1\bar{1}02)$ plane are far more active than others for the photochemical reduction of aqueous Ag^+ to solid Ag^0, and surfaces oriented within 30° of the (0001) plane are far less active than others. The surface potentials of the highly active (poorly active) grains, measured using scanning Kelvin probe microscopy, are more (less) positive than the surface potentials of the other grains. The anisotropy of the activity can be rationalized considering the relative internal fields arising from surface charges along with the bulk absorption and carrier transport, which work together to make the activity of the $(1\bar{1}02)$ plane superior and the activity of the (0001) plane inferior.

Acknowledgments

The authors acknowledge the support of National Science Foundation grant DMR 1206656. The authors acknowledge use of the Materials Characterization Facility at Carnegie Mellon University supported by grant MCF-677785.

Supporting Information

Additional Supporting Information may be found in the online version of this article:

Data S1. The orientation dependence of the photochemical activity of α-Fe_2O_3

References

[1] Y. Lin, G. Yuan, S. Sheehan, S. Zhou, and D. Wang, "Hematite-Based Solar Water Splitting: Challenges and Opportunities," *Energy Environ. Sci.*, **4** [12] 4862–9 (2011).

[2] K. Sivula, F. le Formal, and M. Grätzel, "Solar Water Splitting: Progress Using Hematite (α-Fe_2O_3) Photoelectrodes," *Chemsuschem*, **4** [4] 432–49 (2011).

[3] M. A. Gondal, A. Hameed, Z. H. Yamani, and A. Suwaiyan, "Production of Hydrogen and Oxygen by Water Splitting Using Laser Induced Photo-Catalysis Over Fe_2O_3," *Appl. Catal. A*, **268** [1–2] 159–67 (2004).

[4] J. Y. Cao, T. Kako, N. Kikugawa, and J. H. Ye, "Photoanodic Properties of Pulsed-Laser-Deposited α-Fe_2O_3 Electrode," *J. Phys. D*, **43** [32] 325101, 7pp (2010).

[5] Y. Lin, S. Zhou, S. W. Sheehan, and D. Wang, "Nanonet-Based Hematite Heteronanostructures for Efficient Solar Water Splitting," *J. Am. Chem. Soc.*, **133** [8] 2398–401 (2011).

[6] J. Luo and P. A. Maggard, "Hydrothermal Synthesis and Photocatalytic Activities of $SrTiO_3$-Coated Fe_2O_3 and $BiFeO_3$," *Adv. Mater.*, **18** [4] 514–17 (2006).

[7] A. M. Schultz, P. A. Salvador, and G. S. Rohrer, "Enhanced Photochemical Activity of α-Fe_2O_3 Films Supported on $SrTiO_3$ Substrates Under Visible Light Illumination," *Chem. Comm*, **48** [14] 2012–14 (2012).

[8] Y. Wang, et al., "Enhancement of Photoelectric Conversion Properties of SrTiO3/α-Fe2O3 Heterojunction Photoanode," *J. Phys. D*, **40** [13] 3925–30 (2007).

[9] N. Iordanova, M. Dupuis, and K. M. Rosso, "Charge Transport in Metal Oxides: A Theoretical Study of Hematite α-Fe_2O_3," *J. Chem. Phys*, **122** [14] 144305, 10pp (2005).

[10] D. Benjelloun, J. P. Bonnet, J. P. Doumerc, J. C. Launay, M. Onillon, and P. Hagenmuller, "Anisotropie des Proprietes Electrique de L'oxyde de fer $Fe_2O_3\alpha$," *Mater. Chem. Phys.*, **10** [6] 503–18 (1984).

[11] C. M. Eggleston, A. J. A. Shankle, A. J. Moyer, I. Cesar, and M. Grätzel, "Anisotropic Photocatalytic Properties of Hematite," *Aquat. Sci.*, **71** [2] 151–9 (2009).

[12] R. L. Kurtz and V. E. Henrich, "Surface Electronic Structure and Chemisorption on Corundum Transition-Metal Oxides: A-Fe_2O_3," *Phys. Rev. B*, **36** [6] 3413–21 (1987).

[13] P. Liu, T. Kendelewicz, G. E. Brown Jr, E. J. Nelson, and S. A. Chambers, "Reaction of Water Vapor With α-Al_2O_3(0001) and α-Fe_2O_3(0001) Surfaces: Synchrotron X-ray Photoemission Studies and Thermodynamic Calculations," *Surf. Sci.*, **417** [1] 53–65 (1998).

[14] K. S. Tanwar, J. G. Catalano, S. C. Petitto, S. K. Ghose, P. J. Eng, and T. P. Trainor, "Hydrated α-Fe_2O_3(1102) Surface Structure: Role of Surface Preparation," *Surf. Sci.*, **601** [12] L59–64 (2007).

[15] T. P. Trainor, et al., "Structure and Reactivity of the Hydrated Hematite (0001) Surface," *Surf. Sci.*, **573** [2] 204–24 (2004).

[16] M. A. Henderson, “Insights Into the (1 × 1)-to-(2 × 1) Phase Transition of the α-Fe_2O_3 (012) Surface Using EELS, LEED and Water TPD,” *Surf. Sci.*, **515** [1] 253–62 (2002).

[17] J. G. Catalano, P. Fenter, and C. Park, “Water Ordering and Surface Relaxations at the Hematite (110)–Water Interface,” *Geochim. Cosmochim. Ac*, **73** [8] 2242–51 (2009).

[18] V. Barrón and J. Torrent, “Surface Hydroxyl Configuration of Various Crystal Faces of Hematite and Goethite,” *J. Colloid Interf. Sci*, **177** [2] 407–10 (1996).

[19] R. Munprom, P. A. Salvador, and G. S. Rohrer, “The Orientation Dependence of the Photochemical Reactivity of $BiVO_4$,” *J. Mater. Chem. A*, **3** [5] 2370–7 (2015).

[20] J. B. Lowekamp, G. S. Rohrer, P. A. Morris Hotsenpiller, J. D. Bolt, and W. E. Farneth, “Anisotropic Photochemical Reactivity of Bulk TiO_2 Crystals,” *J. Phys. Chem. B*, **102** [38] 7323–7 (1998).

[21] D. J. Dingley and D. P. Field, “Electron Backscatter Diffraction and Orientation Imaging Microscopy,” *Mater. Sci. Tech*, **13** [1] 69–78 (1997).

[22] R. A. Schwarzer, D. P. Field, B. L. Adams, M. Kumar, and A. J. Schwartz, “Present State of Electron Backscatter Diffraction and Prospective Developments”; pp. 1–20 in *Electron Backscatter Diffraction in Materials Science*, 2nd Edition, Edited by A. J. Schwartz, M. Kumar, B. L. Adams and D. P. Field. Springer, New York, 2009.

[23] J. L. Giocondi and G. S. Rohrer, “Structure Sensitivity of Photochemical Oxidation and Reduction Reactions on $SrTiO_3$ Surfaces,” *J. Am. Ceram. Soc.*, **86** [7] 1182–9 (2003).

[24] A. M. Schultz, Y. Zhang, P. A. Salvador, and G. S. Rohrer, “Effect of Crystal and Domain Orientation on the Visible-Light Photochemical Reduction of Ag on $BiFeO_3$,” *ACS Appl. Mater. Inter*, **3** [5] 1562–7 (2011).

[25] M. Nonnenmacher, M. P. O’Boyle, and H. K. Wickramasinghe, “Kelvin Probe Force Microscopy,” *Appl. Phys. Lett.*, **58** [25] 2921–3 (1991).

[26] S. Mugo and J. Yuan, “Influence of Surface Adsorption on Work Function Measurements on Gold-Platinum Interface Using Scanning Kelvin Probe Microscopy,” *J. Phys: Conf. Ser.*, **371** [1] 012030, 4pp (2012).

[27] E. R. Batista and R. A. Friesner, “A Self-Consistent Charge-Embedding Methodology for ab Initio Quantum Chemical Cluster Modeling of Ionic Solids and Surfaces: Application to the (001) Surface of Hematite (α-Fe_2O_3).,” *J. Phys. Chem. B*, **106** [33] 8136–41 (2002).

[28] M. Rohwerder and F. Turcu, “High-Resolution Kelvin Probe Microscopy in Corrosion Science: Scanning Kelvin Probe Force Microscopy (SKPFM) Versus Classical Scanning Kelvin Probe (SKP).,” *Electrochimi. Acta*, **53** [2] 290–9 (2007).

[29] T. Hochwitz, A. K. Henning, C. Levey, C. Daghlian, and J. Slinkman, “Capacitive Effects on Quantitative Dopant Profiling With Scanned Electrostatic Force Microscopes.,” *J. Vac. Sci. Technol., B*, **14** [1] 457–62 (1996).

[30] A. K. Henning, et al., “Two Dimensional Surface Dopant Profiling in Silicon Using Scanning Kelvin Probe Microscopy.,” *J. Appl. Phys.*, **77** [5] 1888–96 (1995).

[31] D. Ziegler and A. Stemmer, “Force Gradient Sensitive Detection in Lift-Mode Kelvin Probe Force Microscopy.,” *Nanotechnology*, **22** [7] 075501, 9pp (2011).

[32] J. R. Rustad, E. Wasserman, and A. R. Felmy, “Molecular Modeling of the Surface Charging of Hematite: II. Optimal Proton Distribution and Simulation of Surface Charge Versus pH Relationships.,” *Surf. Sci.*, **424** [1] 28–35 (1999).

[33] M. A. Henderson, S. A. Joyce, and J. R. Rustad, “Interaction of Water With the (1 × 1) and (2 × 1) Surfaces of α-Fe 2 O 3 (012).,” *Surf. Sci.*, **417** [1] 66–81 (1998).

[34] G. A. Parks and P. D. Bruyn, “The Zero Point of Charge of Oxides1.,” *J. Phys. Chem.*, **66** [6] 967–73 (1962).

[35] S. V. Yanina and K. M. Rosso, “Linked Reactivity at Mineral-Water Interfaces Through Bulk Crystal Conduction.,” *Science*, **320** [5873] 218–22 (2008).

[36] S. Chatman, P. Zarzycki, and K. M. Rosso, “Surface Potentials of (001), (012),(113) Hematite (α-Fe_2O_3) Crystal Faces in Aqueous Solution.,” *Phys. Chem. Chem. Phys.*, **15** [33] 13911–21 (2013).

[37] S. Kerisit and K. M. Rosso, “Computer Simulation of Electron Transfer at Hematite Surfaces,” *Geochim. Cosmochim. Ac*, **70** [8] 1888–903 (2006).

[38] J. L. Giocondi, P. A. Salvador, and G. S. Rohrer, “The Origin of Photochemical Anisotropy in $SrTiO_3$,” *Top. Catal.*, **44** [4] 529–33 (2007).

[39] M. N. Huda, A. Walsh, Y. Yan, S.-H. Wei, and M. M. Al-Jassim, “Electronic, Structural, and Magnetic Effects of *3d* Transition Metals in Hematite,” *J. Appl. Phys.*, **107** [12] 123712, 6pp (2010).

[40] P. A. Morris Hotsenpiller, J. D. Bolt, W. E. Farneth, J. B. Lowekamp, and G. S. Rohrer, “Orientation Dependence of Photochemical Reactions on TiO_2 Surfaces,” *J. Phys. Chem. B*, **102** [17] 3216–26 (1998).

[41] A. Imanishi, T. Okamura, N. Ohashi, R. Nakamura, and Y. Nakato, “Mechanism of Water Photooxidation Reaction at Atomically Flat TiO_2 (Rutile) (110) and (100) Surfaces: Dependence on Solution pH,” *J. Am. Chem. Soc.*, **129** [37] 11569–78 (2007).

[42] T. Ohno, K. Sarukawa, and M. Matsumura, “Crystal Faces of Rutile and Anatase TiO_2 Particles and Their Roles in Photocatalytic Reactions,” *New J. Chem.*, **26** [9] 1167–70 (2002).

[43] S. Liu, J. Yu, and M. Jaroniec, “Tunable Photocatalytic Selectivity of Hollow TiO_2 Microspheres Composed of Anatase Polyhedra With Exposed {001} Facets,” *J. Am. Chem. Soc.*, **132** [34] 11914–16 (2010).

[44] A. Bhardwaj, N. V. Burbure, A. Gamalski, and G. S. Rohrer, “Composition Dependence of the Photochemical Reduction of Ag by $Ba_{1-x}Sr_xTiO_3$,” *Chem. Mater.*, **22** [11] 3527–34 (2010).

[45] J. L. Giocondi and G. S. Rohrer, “The Influence of the Dipolar Field Effect on the Photochemical Reactivity of $Sr_2Nb_2O_7$ and $BaTiO_3$ Microcrystals,” *Top. Catal.*, **49** [1–2] 18–23 (2008).

[46] Y. Inoue, K. Sato, K. Sato, and H. Miyama, “Photoassisted Water Decomposition by Ferroelectric Lead Zirconate Titanate Ceramics With Anomalous Photovoltaic Effects,” *J. Phys. Chem.*, **90** [13] 2809–10 (1986).

[47] R. Munprom, P. A. Salvador, and G. S. Rohrer, “Polar Domains at the Surface of Centrosymmetric $BiVO_4$,” *Chem. Mater.*, **26** [9] 274–6 (2014).

[48] G. Li, Z. Yi, H. Wang, C. Jia, and W. Zhang, “Factors Impacted on Anisotropic Photocatalytic Oxidization Activity of ZnO: Surface Band Bending, Surface Free Energy and Surface Conductance,” *Appl. Catal. B*, **158–159**, 280–5 (2014). □